



Optimizing the activation efficiency of sub-3 nm particles in a laminar flow condensation particle counter: Model simulation

Weixing Hao ^a, Mark Stolzenburg ^b, Michel Attoui ^c, Jiaoshi Zhang ^d, Yang Wang ^{a,*}

^a Department of Civil, Architectural and Environmental Engineering, Missouri University of Science and Technology, Rolla, MO, USA

^b MRS Consulting, Minneapolis, MN, USA

^c LISA, UMR 7583, Université Paris-Est-Créteil, Université de Paris, Institut Pierre Simon Laplace (IPSL), Créteil, France

^d Center for Aerosol Science and Engineering, Washington University in St. Louis, St. Louis, MO, USA



ARTICLE INFO

Keywords:

Condensation particle counter
Sub-3 nm particles
Simulation
Working fluid
COMSOL

ABSTRACT

The measurement of airborne particles with sizes below 3 nm is critical, as it helps the understanding of atmospheric nucleation and elucidates important particle synthesis mechanisms in the gas phase. Condensation particle counters (CPCs) have been widely used to measure the concentration of aerosols. However, it is challenging for the CPCs to measure particles below 3 nm due to the insufficient activation of these particles via vapor condensation. Methods have been proposed to increase the saturation ratio of the condensing vapor to promote the detection efficiency of sub-3 nm particles in the CPCs. Different working fluids also make a considerable impact on particle detection. Given the various types of parameters and the wide range of values these parameters can take, modeling studies are needed in searching for the optimal operating conditions of a CPC.

In this work, we simulated the sub-3 nm particle activation and growth in a laminar flow CPC using COMSOL Multiphysics®, which has the advantages of simulating complex flow conditions and interfacing with post-processing software such as MATLAB. Our simulation incorporates the influence of temperature-dependent air and working fluid properties on particle activation and the impact of latent heat and non-continuum effects on droplet growth. Following the method introduced by Iida, Stolzenburg and McMurry (2009), particle activation is optimized for a given working fluid and condenser temperature by adjusting the saturation temperature to achieve a homogeneous nucleation rate of 1 s^{-1} . The results, characterized by $D_{\text{kel},0}$ (largest particle size that cannot be activated) and $D_{\text{kel},50}$ (particle size activated with 50% efficiency), were compared against the analytical Graetz model used in Stolzenburg (1988). Our COMSOL simulations show that glycerine, diethylene glycol, ethylene glycol, 2-aminoethanol, and dimethyl phthalate are the best five working fluids achieving the smallest $D_{\text{kel},50}$ among 45 commonly used solvents. The $D_{\text{kel},50}$ values simulated by COMSOL under a condenser temperature of 10 °C for the five working fluids are 1.56, 1.88, 1.92, 1.98, and 2.10 nm, respectively, while the values simulated by the analytical Graetz solution differ slightly from 0.4% to 0.7%. The results demonstrate excellent agreement between these two simulation methods. For the five best working fluids activating the same 2.1 nm particles, the droplets can grow to sizes detectable by a second-stage CPC. The sensitivity of the COMSOL solution to the inlet condition and the form of convective diffusion equations is investigated. We also discussed the effect of CPC operating conditions, such as the

* Corresponding author.

E-mail address: yangwang@mst.edu (Y. Wang).

condenser geometry and flow conditions, on particle activation for optimizing the performance of the CPC in detecting sub-3 nm particles.

Nomenclature

c	Molecular concentration of the condensing vapor [mol m ⁻³]
c_p	Heat capacity of the working fluid [J K ⁻¹ kg ⁻¹]
$c_{p,g}$	Heat capacity of air [J K ⁻¹ kg ⁻¹]
D	Diffusivity of the condensing vapor [m ² s ⁻¹]
D_c	Diameter of the condenser [m]
D_p	Particle size [m]
$D_{p,kel}$	Size of particle that can be activated according to the Kelvin equation [m]
$D_{p,kel,0}$	Smallest size of particle that can be activated in the CPC [m]
$D_{p,kel,50}$	Size of particle that has a 50% activation efficiency [m]
H_{vap}	Heat of vaporization of the working fluid [J kg ⁻¹]
I	nucleation rate [m ⁻³ s ⁻¹]
k	Boltzmann constant, 1.38×10^{-23} [J K ⁻¹]
k_g	Thermal conductivity of gaseous phase [W m ⁻¹ K ⁻¹]
L_c	Length of the condenser [m]
L_s	Length of the saturator [m]
m	Molecular mass of the working fluid [kg]
m_g	Molecular mass of air [kg]
n	Molecular concentration of the condensing vapor [molecules m ⁻³]
N	Concentration of the particles [particles m ⁻³]
N_0	Concentration of the particles at the outlet of the capillary [particles m ⁻³]
p	Partial pressure of the condensing vapor [Pa]
p_d	Equilibrium condensing vapor pressure at the surface of the droplet [Pa]
p_s	Saturation vapor pressure of the condensing vapor [Pa]
Q_a	Flow rate through the capillary [m ³ s ⁻¹]
Q_c	Flow rate through the condenser [m ³ s ⁻¹]
r	Radial coordinate in the CPC [m or as otherwise explicitly designated]
R_{act}	Maximum radius of the contour corresponding to $D_{p,kel} = D_p$ [m]
S	Saturation ratio [1]
T	Temperature in the CPC [K]
T_c	Condenser temperature [K]
T_d	Temperature at the surface of the droplet [K]
T_s	Saturator temperature [K]
v_m	Molecular volume of the condensing vapor [m ³]
w	Velocity along the axial direction in the CPC [m s ⁻¹]
z	Axial coordinate in the CPC [m or as otherwise explicitly designated]
Z_{act}	Axial location corresponding to $r = R_{act}$ [m]
α_T	Thermal accommodation coefficient [1]
η_{act}	Activation efficiency [1]
ρ	Density of the working fluid [kg m ⁻³]
ρ_g	Density of air [kg m ⁻³]
σ	Surface tension of the working fluid [N m ⁻¹]
μ	Dynamic viscosity of the working fluid [kg m ⁻¹ s ⁻¹]
χ	Correction factor for non-continuum effects in particle condensational growth [1]
χ_h	Correction factor for non-continuum effects in particle heat transfer [1]

1. Introduction

Aerosol science and technology enable continual advances in material synthesis and atmospheric pollutant control. Among these advances, one important frontier is characterizing the initial stages of particle formation by real-time measurement of particles below 3 nm in size. Sub-3 nm particles play important roles by acting as seeds for particle formation and subsequent growth, ultimately determining the final properties of the generated particles. Tailoring nanoparticle properties requires a thorough understanding and

precise control of the particle formation processes, which in turn requires characterizing nanoparticle formation from the initial stages (Becquemin et al., 1991; Biswas et al., 2018; Wang et al., 2015).

Conventional aerosol instruments start to face difficulties in characterizing particles with sizes below 3 nm. For example, commonly used condensation particle counters (CPCs, e.g., Model 3776 and 3025A, TSI Inc.) cannot detect particles smaller than 2.5 nm, so the early stages of particle formation, such as nucleation and condensation, cannot be observed directly (Jiang et al., 2011). The high diffusivity of sub-3 nm particles also causes higher losses and degradation of resolution for mobility sizing techniques, leading to challenges in interpreting the measurement data (Jiang et al., 2011; Stolzenburg, 1988; Wang et al., 2014). These issues directly led researchers to design advanced aerosol instruments that help us uncover the initial stages of aerosol formation in both the atmospheric environment and laboratory studies.

Among various aerosol properties, aerosol concentration is a critical parameter for evaluating the evolution and impact of aerosols. By coupling concentration measurement with size classification, the size distribution of aerosols is obtained. Particle concentrations are frequently measured by CPCs (Hermann et al., 2007; Kangasluoma & Attoui, 2019; Mordas et al., 2008; Quant et al., 1992; Sem, 2002; Wiedensohler et al., 1997), which grow a sampled particle by condensing the vapor of a working fluid on the surface of the particle until it has an optically detectable size ($\sim 1 \mu\text{m}$) (Stolzenburg, 1988). The smallest particle that can be condensationally grown (or activated) is determined by the Kelvin equation, which considers the effect of the saturation ratio, surface tension, temperature, and molecular volume of the working fluid (Friedlander, 2000). The Kelvin equation dictates that the commonly used butanol-based CPCs have the smallest detectable size of 2.5 nm. Operational factors that can optimize the detection efficiency of CPCs for sub-3 nm particles have been explored in multiple previous studies (Attoui & Kangasluoma, 2019; Mertes et al., 1995; Petäjä et al., 2006; Tuch et al., 2016). Although changing the CPCs working conditions, such as the saturator temperature, condenser temperature, and flow rates, could further lower the detectable size by changing the spatial distribution of the supersaturation profile, the improvement is not significant (Kuang, Chen, McMurry, & Wang, 2012). This is mainly because the onset supersaturation for particle formation by homogeneous nucleation is similar to the heterogeneous onset supersaturation for sub-3 nm particles (Barmpounis et al., 2018). Homogeneous nucleation in the CPCs will lead to the production of aerosols in the CPCs, which will lead to inaccurate measurement of the sampled aerosol concentrations.

Another method to improve the CPCs detection efficiency is to use different types of working fluids. A detailed calculation using the Kelvin equation and the data of more than 800 organic compounds suggests that working fluids with a higher surface tension and a lower vapor pressure could activate smaller particles (Iida et al., 2009). This study also found that diethylene glycol (DEG) is the best candidate working fluid for activating the condensational growth of sub-3 nm particles. However, because of the low vapor pressure of the DEG, the grown particles are not large enough to be directly detected by the optical components in the CPCs. Hence, two-stage CPCs were developed, where the first stage uses DEG to grow particles to a moderate size, and the second stage uses butanol to measure the concentration of the grown particles (Jiang et al., 2011). This design directly led to the manufacture of the two newest types of CPC first stages, the particle size magnifier (PSM, Model A11 CNC-system, Airmodus Ltd.) and the Nano Enhancer (Model 3777, TSI Inc.). Similar to DEG, dimethyl phthalate (DMP) was also introduced as a new working fluid, with discussions on saturation vapor pressure, false counts and detection efficiency (Iida et al., 2019). A finding of water-based laminar-flow CPCs shows that the condensation heat release and vapor depletion associated with particle activation and growth lowers the peak supersaturation (Lewis et al., 2013). Although the activation of sub-2 nm particles is still strongly dependent on the chemical composition of the sampled particles (Iida et al., 2009; Kangasluoma et al., 2014; Thomas et al., 2018), a careful calibration of the system with the tested particle composition can effectively extend the detectable size to 1 nm. These modifications greatly facilitate the observation of particle formation and growth in the initial stages (Bianchi et al., 2016; Wang et al., 2017; Yao et al., 2018).

Due to the complex matrix of parameters in the CPCs and a lack of direct analytical solutions for particle activation, modeling studies are necessary for optimizing the detection efficiency of CPCs. Until now, the most widely used model was developed by Stolzenburg (1988), which solves the CPC heat and mass transfer problem with an analytical Graetz solution that does not consider the capillary inlet geometry and axial diffusion in the CPC. Although this approximation greatly simplifies the solution to the CPC problem, it is unknown whether the approximation may lead to different particle activation. COMSOL Multiphysics® has been used extensively in simulating coupled heat, mass, and momentum transfer problems associated with complex geometries. But until now, relatively few studies examined the CPC performance with COMSOL. Kangasluoma et al. (2015) investigated the effect of temperature difference between the saturator and condenser on the CPC performance by examining the supersaturation field simulated by COMSOL. Using COMSOL, Barmpounis et al. (2018) showed that the detection efficiency of sub-3 nm particles can be improved by lowering the temperature range over which the CPCs operate. Thomas et al. (2018) also used COMSOL to examine how the gas composition affects the particle activation in the CPCs. However, these studies have not compared the simulation results with the widely used Graetz solution, and it is unclear whether these studies considered the effects of inlet geometry and axial diffusion in the simulation.

In this work, we studied the sub-3 nm particle activation and growth in a laminar flow CPC simulated by COMSOL. The simulation incorporated the impact of temperature-dependent fluid properties on particle activation and the effect of latent heat and non-continuum effects on droplet growth. The detection efficiency of sub-3 nm particles was compared between the approximate analytical Graetz solution and the COMSOL model. The effects of the inlet geometry and axial diffusion on particle activation were also examined. The effects of CPC operating conditions such as saturator and condenser temperature, working fluid conditions, the capillary geometry, and flow ratio on particle activation and droplet growth of sub-3 nm particles are also discussed in this study. The results of this study will be used for further optimizing the performance of CPCs for detecting sub-3 nm particles.

2. Methods

2.1. COMSOL setup

A two-dimensional axisymmetric model has been developed in COMSOL Multiphysics 5.3a simulation software. The heat, momentum, and mass transfer equations are solved for incompressible flow. The CPC follows the geometry of Stolzenburg and McMurry (1991), which is composed of a laminar flow tube that can be separated into a saturator extension and a condenser operated under different wall temperatures (Fig. 1a). At the inlet of the saturator extension, sampled aerosols are delivered by a capillary and merged with the particle-free air that is saturated with the vapor of the working fluid. Under the default simulation condition, the condenser tube diameter (D_c) is 4 mm, the saturator extension length (L_s) is 20 mm, the condenser length (L_c) is 80 mm, the condenser temperature (T_c) is 10 °C, the capillary flow temperature (T_a) is 20 °C, the condenser flow rate (Q_c) is 0.3 lpm, and the capillary flow rate (Q_a) is 0.03 lpm. To study how CPC performance depends on these parameters, we also simulated the CPC geometry and working conditions with a wide range of values, as discussed in Section 2.2. Particle activation within the CPC depends on the spatial profile of saturation ratio (S) of the condensing vapor, which is calculated by

$$S = \frac{p}{p_s} \quad (1)$$

where p is the partial pressure of the condensing vapor at any location of the CPC, and p_s is the saturation vapor pressure of the condensing vapor, which is further a function of temperature as shown in Table 1. The coupled heat transfer and fluid flow is solved by the conjugate heat transfer module of COMSOL, while the mass transfer of the condensing vapor, or the convective diffusion equation, is solved based on the temperature and flow field solved by the conjugate heat transfer. The particles are introduced from the inlet of the capillary, and are also treated as a diluted species that follow convective diffusion equation in the simulation. Here, we assume that the partial pressure of the condensing vapor at the inlet of the saturator extension (except in the capillary) and at the wall of the

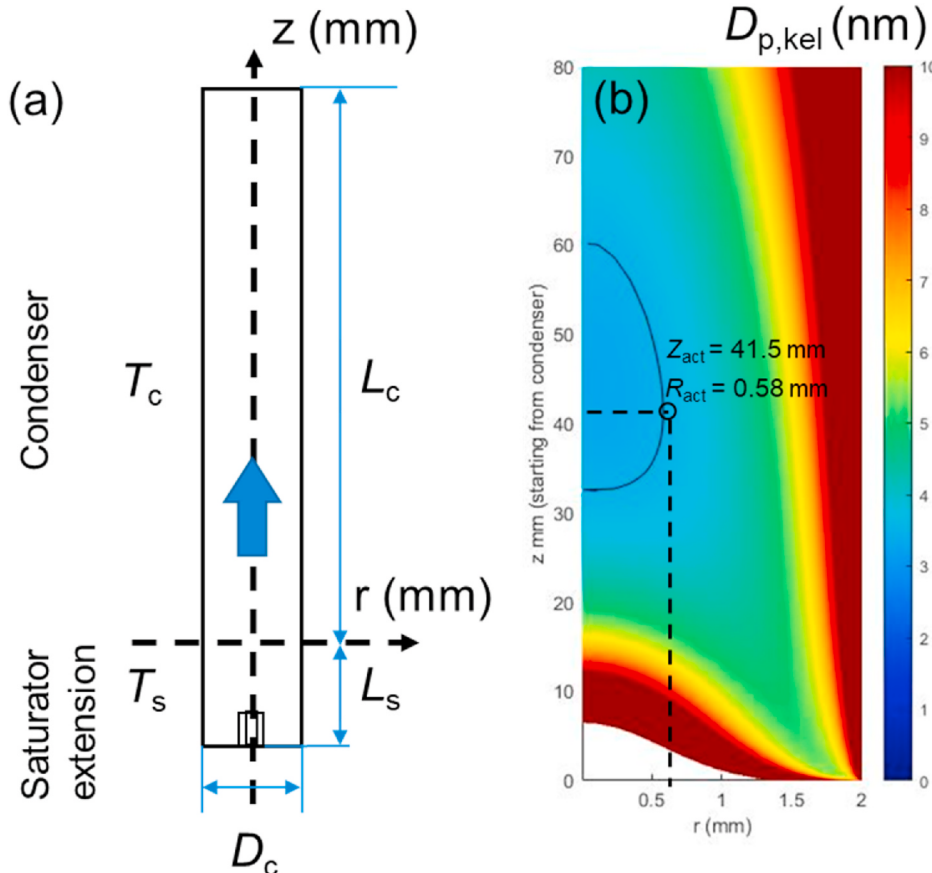


Fig. 1. (a) Geometry of the CPC used in COMSOL simulation. The capillary located at the entrance of the saturator has a length of 1 mm, an inner diameter of 0.5 mm, and an outer diameter of 1.26 mm and (b) equilibrium Kelvin diameter ($D_{p,\text{kel}}$, color contour plot) with the contour line (black curve) corresponding to $D_{p,\text{kel}} = 3.5$ nm. The maximum radius of the contour (R_{act}) and axial coordinate (Z_{act}) corresponding to $r = R_{\text{act}}$ are also labeled. (For interpretation of the references to color in this figure legend, the reader is referred to the Web version of this article.)

Table 1

Parameters of the working fluids as determined from Yaw's handbook. B, G, DEG, EG, 2AE, and DMP stand for 1-butanol, glycerine, diethylene glycol, ethylene glycol, 2-aminoethanol, and dimethyl phthalate, respectively. T stands for temperature in K.

Properties		$p_s = 101325/760 \times 10^{A+\frac{B}{T} + C\ln(T) + DT + ET^2}$														
Type	p_s (Pa)	σ ($N\ m^{-1}$)					ρ ($kg\ m^{-3}$)				D ($m^2\ s^{-1}$)					
		A	B	C	D	E	A	T_c	n	A	B	n	T_c	A	B	C
B		3.97×10^1	-4.00×10^3	-1.03×10^1	-3.26×10^{-10}	8.67×10^{-7}	6.45×10^1	563	1.22	2.69×10^{-1}	2.67×10^{-1}	2.46×10^{-1}	563	-4.65×10^{-2}	2.72×10^{-4}	5.81×10^{-7}
G		1.55×10^1	-4.53×10^3	-1.67×10^0	0	0	1.25×10^2	723	1.22	3.49×10^{-1}	2.49×10^{-1}	1.54×10^{-1}	723	-4.62×10^{-2}	2.50×10^{-4}	6.00×10^{-7}
DEG		6.51×10^0	-4.61×10^3	4.63×10^0	-1.84×10^{-2}	8.29×10^{-6}	9.26×10^1	745	1.22	3.40×10^{-1}	2.61×10^{-1}	2.42×10^{-1}	745	-4.22×10^{-2}	2.28×10^{-4}	5.31×10^{-7}
EG		8.24×10^1	-6.35×10^3	-2.54×10^1	-2.37×10^{-9}	8.75×10^{-6}	1.06×10^2	645	1.22	3.25×10^{-1}	2.55×10^{-1}	1.72×10^{-1}	645	-5.76×10^{-2}	3.17×10^{-4}	7.15×10^{-7}
2AE		7.29×10^1	-5.86×10^3	-2.19×10^1	-7.15×10^{-10}	5.98×10^{-6}	1.08×10^2	638	1.22	2.72×10^{-1}	2.24×10^{-1}	2.02×10^{-1}	638	-5.49×10^{-2}	3.14×10^{-4}	6.96×10^{-7}
DMP		1.27×10^1	-4.20×10^3	3.46×10^{-1}	-7.65×10^{-3}	3.35×10^{-6}	7.51×10^1	766	1.25	3.66×10^{-1}	2.54×10^{-1}	3.07×10^{-1}	766	-3.06×10^{-2}	1.62×10^{-4}	3.88×10^{-7}

saturator extension and condenser is saturated ($S = 1$).

Although commercial CPCs set saturator temperature at fixed values, in this study, unless stated otherwise, we used an iteration method that finds the optimal saturator temperature (T_s) value corresponding to a total homogeneous nucleation rate of one particle per second (1 s^{-1}) within the condenser (Iida et al., 2009). This method would guarantee a highest possible supersaturation in the CPC which can optimize the activation efficiency of sub-3 nm particles. According to particle number conservation, under steady state, the flux of homogeneously nucleated particles at the exit of the condenser or through the optics region of the CPC equals the rate of particles being generated in the condenser. Therefore, under the optimized saturator temperature, the contribution of homogeneously nucleated particles to total detected particles will be limited to 1 s^{-1} . Note that similar to the condensation of vapor species, homogeneous nucleation also depends on fluid properties such as surface tension, vapor pressure, molar volume, etc., (as shown in Section 3.2), meaning that the optimized saturator temperature varies with different working fluids. Figs. S1a and S1b show examples of temperature and saturation ratio profiles within the simulated geometry under the default condition while $T_s = 40^\circ\text{C}$.

With the spatial profile of S , we can further calculate the particle activation, homogeneous nucleation, and condensational growth. The Kelvin equivalent size ($D_{p,\text{kel}}$) is the minimum diameter of particles that can be activated for condensation growth. It is determined by the surface tension (σ), molecular volume (v_m), temperature (T), Boltzmann constant (k), and saturation ratio (S),

$$D_{p,\text{kel}} = \frac{4\sigma v_m}{kT \ln(S)} \quad (2)$$

When particle size (D_p) is above $D_{p,\text{kel}}$, the particle can be successfully activated and grown by vapor condensation, and when D_p is below $D_{p,\text{kel}}$, the particles cannot be activated. One needs to note that due to the spatial variation of T , σ , and S (e.g., Figs. S1a and S1b), $D_{p,\text{kel}}$ also varies at different locations of the condenser (Fig. 1b). Particles near the wall of the condenser, where there is a lower S , are more difficult to activate due to the larger $D_{p,\text{kel}}$.

The simulated temperature and concentration fields were then imported into MATLAB and interpolated at any given point in the r - z plane. The activation efficiency of particles with a size of D_p is derived using the similar approach in Stolzenburg and McMurry (1991), which is briefly introduced as follows. First, the contour line corresponding to $D_{p,\text{kel}} = D_p$ can be drawn from the contour plot of $D_{p,\text{kel}}$. Second, the maximum radius (R_{act}) of the contour is determined, and the axial location corresponding to R_{act} is denoted as Z_{act} (Fig. 1b). Therefore, at $z = Z_{\text{act}}$, particles with radial location of $r \leq R_{\text{act}}$ can be activated. Third, the activation efficiency is calculated by

$$\eta_{\text{act}} = \frac{\int_0^{R_{\text{act}}} 2\pi r w N dr}{Q_a N_0} \quad (3)$$

where w is the velocity along the axial direction and N is the concentration of particles, both at the axial location of $z = Z_{\text{act}}$. N_0 is the particle concentration at the outlet of the capillary. η_{act} therefore depends on D_p , and by calculating and plotting η_{act} as a function of D_p , we can obtain the activation efficiency curve under the operating conditions of the CPC. Note here that the calculation of the activation efficiency in Eq. (3) also considers the diffusion loss of the particles in the condenser. On the activation curve, two points are of interest. They are $D_{p,\text{kel},0}$, which is the largest particle size that cannot be activated in the condenser (0% activation efficiency), and $D_{p,\text{kel},50}$, which is the size of particle having 50% activation efficiency. $D_{p,\text{kel},50}$ is of great importance for the performance of a CPC, as it determines the general particle size range in which the CPC can confidently measure. As discussed earlier, the saturator temperature setting depends on the homogeneous nucleation rate (I) (Friedlander, 2000), which is calculated by

$$I = 2 \times \left[\frac{p}{(2\pi mkT)^{1/2}} \right] \times \left(nv_m^{2/3} \right) \times \left[\frac{\sigma v_m^{2/3}}{kT} \right]^{1/2} \times \exp \left[-\frac{16\pi\sigma^3 v_m^2}{3(kT)^3 (\ln S)^2} \right] \quad (4)$$

where m is the molecular mass of the working fluid and n is the molecular concentration of the condensing vapor. The total nucleation rate within the condenser is calculated by integrating I within the volume of the condenser.

Once the particles are activated, their condensational growth along their trajectories can be estimated with

$$\frac{dD_p}{dt} = \frac{4Dv_m\chi}{kT} \frac{(p - p_d)}{D_p} \quad (5)$$

where D is the diffusivity of the condensing vapor molecule, and p_d represents the equilibrium condensing vapor pressure at the surface of the droplet, which is calculated by $p_d = p_s(T_d) \exp \left(\frac{4\sigma v_m}{kT_d D_p} \right)$ (Butt et al., 2013). χ corrects for the non-continuum effect of the particles, and is calculated with $\chi = \frac{1+\text{Kn}}{1+1.71\text{Kn}+1.333\text{Kn}^2}$ (Hegg & Larson, 1990), where Kn is the Knudsen number ($\text{Kn} = 2\lambda/D_p$, λ is the mean free path of vapor molecules in air). To estimate the heat transfer and the droplet surface temperature (T_d), we consider the temperature difference between the surrounding air (T) and the droplet surface and the latent heat of vaporization. T_d is governed by

$$\frac{dT_d}{dt} = \frac{3}{c_p \rho D_p} \left(H_{\text{vap}} \rho \frac{dD_p}{dt} - 4k_g \frac{(T_d - T)\chi_h}{D_p} \right) \quad (6)$$

where c_p , ρ , and H_{vap} are the heat capacity, density, and heat of vaporization of the working fluid. k_g is the thermal conductivity of air.

χ_h corrects for the non-continuum effects in heat transfer, and it is given by $\chi_h = \left[1 + \frac{2k_g}{\alpha_T D_p \rho_g c_{p,g}} \left(\frac{2\pi m_g}{kT} \right)^{1/2} \right]^{-1}$, where m_g , ρ_g , and $c_{p,g}$ are the molecular weight, density, and heat capacity of air, respectively. α_T is the thermal accommodation coefficient, and was assumed to be unity (Seinfeld and Pandis, 2016). For the simulation of droplet growth, we assume that particles move along the axial direction of the CPC (no movement in the radial direction) with a speed of w . Therefore, Eqs. (5) and (6) can be converted to a function of axial location using $w = dz/dt$, and the droplet size at the end of the condenser ($z = L_c$) can be calculated.

The Graetz solution to the heat and mass transfer in the CPC was used as a reference to evaluate the accuracy of the COMSOL simulation in particle activation calculation. In the Graetz solution, the flow at the inlet of the saturator extension is assumed to be fully developed, meaning that the capillary geometry was neglected. The properties of the working fluids are also evaluated at a reference temperature (25 °C) throughout the simulated geometry to simplify the calculation. The Graetz solution does not account for axial diffusion, which is usually negligible due to the relatively small gradient of temperature and concentrations along the axial direction. Furthermore, the Graetz solution used in Stolzenburg and McMurry (1991) solved the convective diffusion equation using vapor partial pressure (p) as the variable, whereas the mass transfer module in COMSOL uses vapor concentration (c) as the variable. According to the ideal gas law, these two methods are the same if the temperature is a constant in the simulated geometry. However, this assumption does not hold due to the different temperature settings of the saturator and condenser. It is therefore also necessary to examine how the use of different variables in the convective diffusion equation may affect the particle activation efficiency. Note that the reason for using partial pressure instead of vapor concentration in the Graetz solution is that, for mixtures of gases, one generally uses fugacity rather than chemical potential to analyze the mass transport. For an ideal mixture, fugacity is equal to partial pressure (Atkins & De Paula, 2006; Ewing et al., 1994).

2.2. Simulation plan

Table 2 lists the parameters in each simulation task of this study. Before applying COMSOL for more complex tasks, we first compared the COMSOL solution against the Graetz solution (Task 1), which neglects the inlet geometry, axial diffusion, and the temperature dependence of the working fluid properties, and uses vapor partial pressure as the variable in the convective diffusion equation. Since the mass transfer module in COMSOL considers axial diffusion (while the remaining parameters were tuned to be the same as the Graetz model), the comparison between the Graetz and COMSOL solutions also provides an estimate of the effect of axial diffusion on particle activation. In Task 2, we include the geometry of the capillary at the inlet of the saturator extension, which has inner and outer diameters of 0.50 mm and 1.26 mm, and a length of 1 mm (Stolzenburg, 1988). The presence of the capillary increases the average flow velocity at the inlet of the saturator extension, since the wall of the capillary tube reduced the cross sectional area for the passage of the saturator flow. Tasks 2 and 3 examine how using different variables for the convective diffusion equation affects the particle activation efficiency calculation. Tasks 1–3 also assume a constant T_s of 40 °C.

In Task 4, we examined the performance of the CPC using 46 different types of common and affordable solvents as working fluids (ACS Division of Organic Chemistry, 2020). These solvents have boiling points above 50 °C and freezing points below –10 °C, which suits the usage under general ambient conditions. Here, we considered the influence of the temperature-dependent thermodynamic properties, which are obtained from Yaws and Gabbula (2003). T_s is optimized using the iteration method to ensure a highest detection efficiency of sub-3 nm particles. This study selected five working fluids that have the best performance in sub-3 nm particle detection (as discussed in Section 3.2), which are glycerin, diethylene glycol, ethylene glycol, 2-aminoethanol, and dimethyl phthalate, and their thermodynamic properties are listed in Table 1. Tasks 5–9 further tested how the CPC working conditions, such as T_c , Q_c , Q_a , D_c , and L_c , affect the performance of the CPC. These calculations reveal optimal working conditions that can further enhance the detection of sub-3 nm particles.

Table 2

Parameters of CPC for different simulation tasks. Note: O is for optimal saturator temperature (T_s) value corresponding to a total homogeneous nucleation rate of one particle per second (1 s^{-1}) within the condenser. B stands for butanol.

Task	T_c (oC)	T_s (oC)	Q_c (lpm)	Q_a (lpm)	D_c (mm)	L_c (mm)	Fluid	Capillary	Variable
1	10	40	0.3	0.03	4	80	B	No	p
2	10	40	0.3	0.03	4	80	B	Yes	p
3	10	40	0.3	0.03	4	80	B	Yes	c
4	10	O	0.3	0.03	4	80	46 types	No	p
5	–5–15	O	0.3	0.03	4	80	B	Yes	p
6	10	O	0.1–0.9	0.1Qcon	4	80	B	Yes	p
7	10	O	0.3	0.01–0.09	4	80	B	Yes	p
8	10	O	0.3	0.03	2–6	80	B	Yes	p
9	10	O	0.3	0.03	4	40–120	B	Yes	p

3. Results and discussion

3.1. Performance of the COMSOL simulation

A comparison between the COMSOL and Graetz solutions for the profiles of temperature, condensing vapor partial pressure, and saturation ratio at two different radial locations ($r = 0 \text{ mm}$ and 1 mm (50% of the condenser radius)) of the CPC is shown in Fig. 2. The two simulation methods showed excellent agreement between each other. Because of the almost identical profiles of temperature, partial pressure, and saturation ratio, the activation efficiencies as a function of particle size calculated by the two methods are also very similar, as shown in Fig. 2d. Based on the activation efficiency curve, we can further derive that $D_{p,\text{kel},50}$ for butanol at $T_s = 40^\circ\text{C}$ and $T_c = 10^\circ\text{C}$ are 3.44 nm for both the Graetz and COMSOL solutions. The agreement between these two simulation methods also shows that axial diffusion can be neglected due to the relatively low gradient in temperature and concentrations along the axial direction of the CPC.

Fig. 2 also shows the development of the spatial profiles of the thermodynamic properties in the CPC. In the saturator extension ($-20 \text{ mm} \leq z \leq 0$), the temperature is the highest due to the confluence of the particle-free air from the saturator operated at a higher temperature. Along the centerline of the CPC, the temperature increases rapidly within the saturator extension from 293 K to 311 K, which is close to the temperature at $r = 1 \text{ mm}$ at the outlet of the saturator extension ($z = 0$). However, this rapid increase of the temperature may be slowed down under higher condenser flow rates or higher aerosol flow fractions. In the condenser, due to the colder wall temperature, the temperature away from the centerline cools down more rapidly compared to the centerline. This more rapid decrease at the location away from the centerline was also observed in the profile of butanol vapor partial pressure. However, because the diffusivity of the butanol vapor is smaller than the heat diffusivity, the decrease of the temperature is more rapid than that of the vapor partial pressure. This more rapid diffusion of the temperature, and hence, p_s , along with the non-linearity of the p_s and T relationship, creates saturation ratios higher than 1 in the condenser, as illustrated in Fig. 2c, where the maximum S along the centerline is higher compared to that away from the centerline.

Fig. 3 shows how the incorporation of the actual capillary geometry affects the profiles of thermodynamic properties and the activation efficiency. The introduction of the capillary geometry causes some flow disturbance in the flow profile and the development

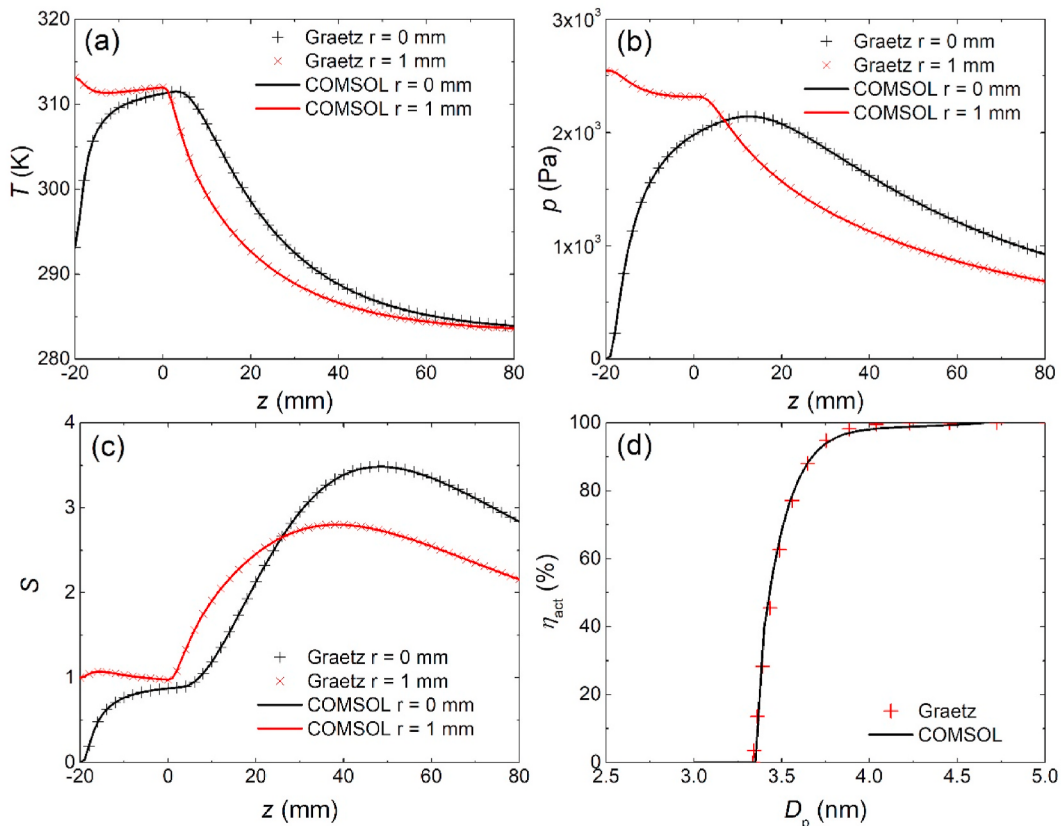


Fig. 2. Comparison between COMSOL and Graetz solutions for (a) temperature (T), (b) vapor pressure (p), (c) saturation ratio (S), and (d) activation efficiency as a function of particle diameter. Note that the inlet geometry and the temperature dependence of the working fluid properties are neglected. Both simulations used vapor partial pressure as the variable in the convective diffusion equation.

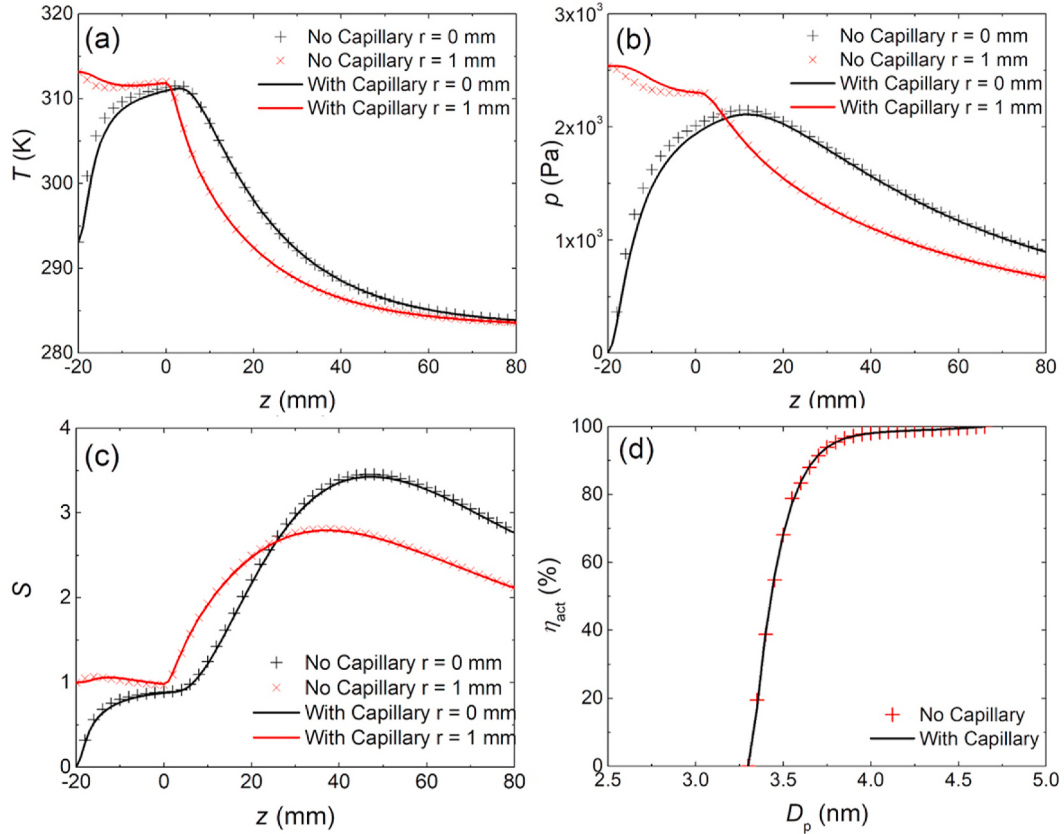


Fig. 3. Effect of the capillary geometry on (a) temperature (T), (b) vapor pressure (p), (c) saturation ratio (S), and (d) activation efficiency as a function of particle diameter.

of the temperature and vapor pressure profiles. However, the disturbances largely dissipate by the end of the saturator extension, where the T and p profiles are nearly flat as shown in Fig. 3a and b. Therefore, including the capillary geometry would have a limited effect on the results in the condenser. Moreover, in the design of the CPC capillary, the diameter of the capillary was designed so that the aerosol flow rate through the capillary equals that through an imaginary disc with the same diameter as the capillary outer diameter under a fully developed parabolic flow profile. Such a design would ensure a minimal flow turbulence and dispersion of the aerosols, so that the aerosols can be restricted in regions with a high saturation ratio. For comparison with Fig. 2d, the activation efficiency curves for conditions with and without the capillary geometry are shown in Fig. 3d. Size of particle that can be activated in the CPC from the axis of the condenser is shown in Fig. S2a.

When c is used as the variable to solve the convective diffusion equation, similar to that in Barmpounis et al. (2018), the profiles of the thermodynamic properties and activation efficiency are noticeably different from that using p as the variable (Fig. 4). This large difference is due to the large temperature variation in the simulated system. According to the ideal gas law ($p = cRT$), temperature and concentration would both affect the gradient of partial pressure, ultimately affecting the flux of vapor through diffusion. The $D_{p,kel,0}$ derived by using c as the variable is approximately 0.3 nm larger than that using p as the variable in the convective diffusion equation, but the axial locations corresponding to $D_{p,kel,0}$ are the same. Due to the varying temperature field, solving the convective diffusion equation with different variables can result in differences in the simulated activation efficiencies (Fig. 4d). Size of particle that can be activated in the CPC from the axis of the condenser is also shown in Fig. S2b. Therefore, results obtained from the COMSOL mass transport module (transport of diluted species) should not be directly compared against that obtained from the Graetz solution. For consistency, we will use the method of Stolzenburg (1988) with the Graetz solution, which solves the convective diffusion equation using p as the variable in the following analysis.

3.2. Influence of the working fluid

Working fluids play a significant role in the CPC performance in measuring sub-3 nm particles. In this work, using the method similar to Iida et al. (2009), we examined the dependence of $D_{p,kel,50}$ on the thermodynamic properties of working fluids with a focus on saturation vapor pressure (p_s) and surface tension (σ), which directly affect the mass transfer of the vapor and activation of the particles (Fig. 5). We examined whether the performance of the CPC would rely on saturator temperature (T_s) (Fig. S3a), which is

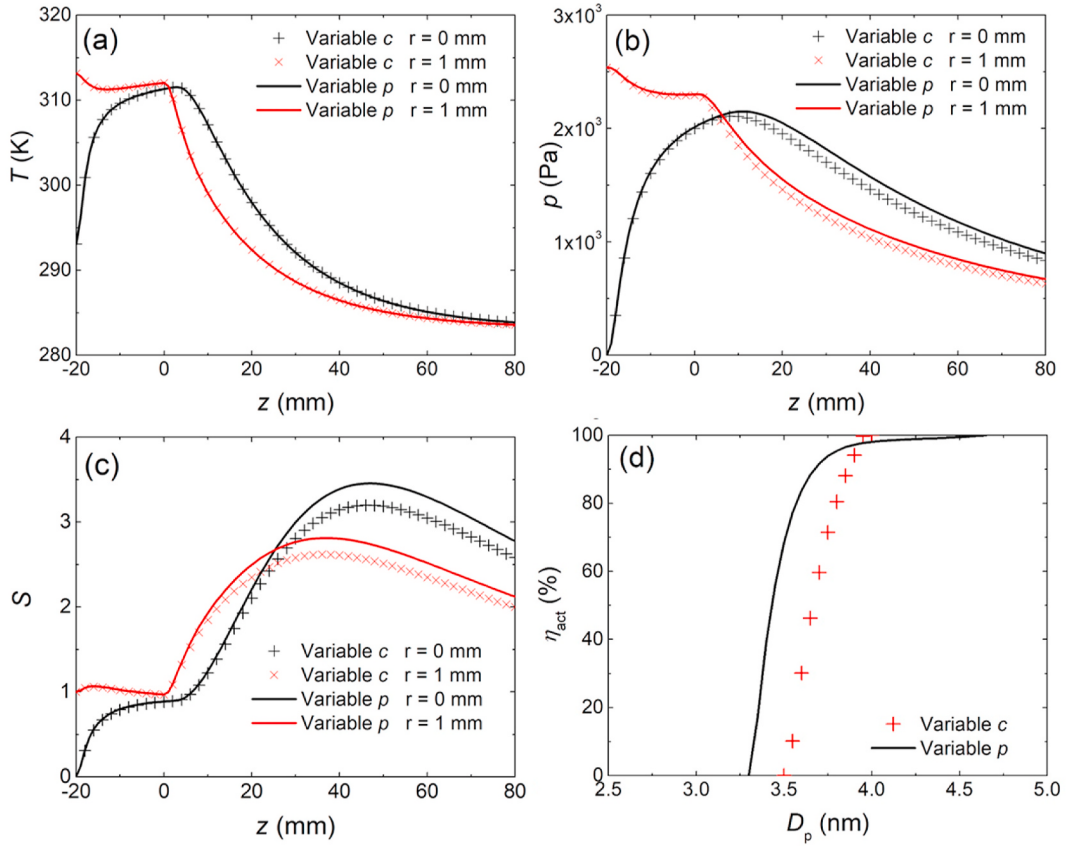


Fig. 4. Effect of using c and p as the variable to solve for the convective diffusion equation on (a) temperature (T), (b) vapor pressure (p), (c) saturation ratio (S), and (d) activation efficiency as a function of particle diameter.

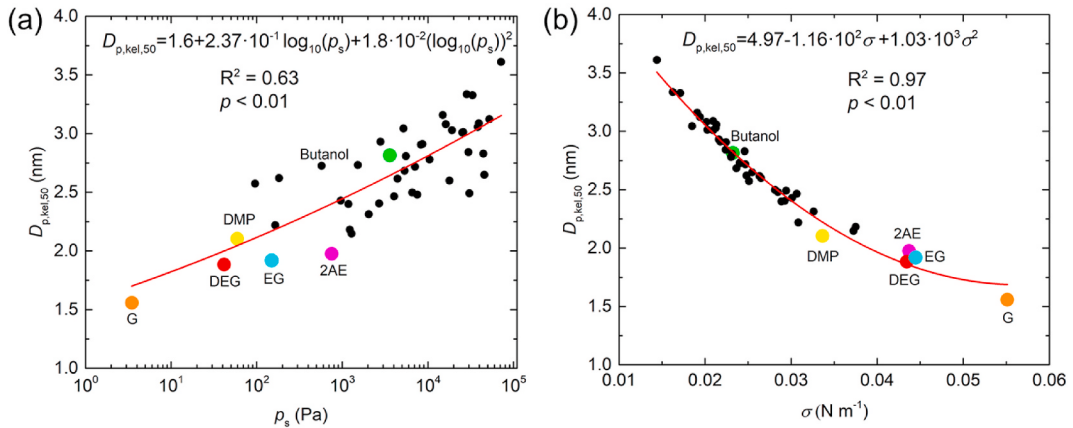


Fig. 5. Effect of the (a) saturation vapor pressure (p_s) and (b) surface tension (σ) on particle size activated with 50% efficiency ($D_{p,kel,50}$). G, DEG, EG, 2AE, and DMP stand for glycerine, diethylene glycol, ethylene glycol, 2-aminoethanol, and dimethyl phthalate, respectively.

optimized to achieve the highest saturation ratio. Since viscosity (μ) will affect the convenience of wetting the wick of the CPCs, we also examined the viscosity of the working fluid and plotted the values against $D_{p,kel,50}$ (Fig. S3b). The effect of working fluid density (ρ) and vapor molecule diffusivity (D) are also plotted (Figs. S3c and S3d). We identified the five best working fluids that could achieve the lowest $D_{p,kel,50}$, which, together with butanol, are distinguished with different colors in Fig. 5 and Fig. S3. The scattered data was also fitted with 2nd order polynomial equations, which are displayed in each panel of the figure along with the probability of the null hypothesis (no correlation) being true.

The results show that the lower $D_{p,\text{kel},50}$ correlates with a lower p_s and a higher σ , a finding that is in agreement with the earlier work by Iida et al. (2009). According to Eq. (4), a higher σ and a larger molecular volume would enhance the evaporation of the condensing vapor from tiny clusters that are smaller than the sampled aerosols, thereby suppressing the rate of homogeneous nucleation. A lower p_s could reduce the collision rates among the condensing vapor molecules, suppressing the rate of homogeneous nucleation. This reduced rate means that T_s can be raised further to enhance the saturation ratio in the condenser, leading to a smaller $D_{p,\text{kel},50}$. Although T_s is a derived parameter in this calculation, and it is not an input or control parameter, the correlation shows in general that working fluids with higher T_s can have smaller $D_{p,\text{kel},50}$. ρ and μ negatively correlate with $D_{p,\text{kel},50}$, resulting from their negative correlation with p_s . That is, higher ρ and μ correspond to increasing intermolecular forces in the condensed phase and therefore lower p_s . Hence, the wetting of the CPC wick may be more challenging with working fluids having lower $D_{p,\text{kel},50}$. Since D is a property associated with transport phenomena, not equilibrium, D does not have a noticeable influence on particle activation (Fig. S3d). Note that, although the exact $D_{p,\text{kel},50}$ values would rely on other CPC operating conditions such as the condenser temperature and the CPC geometry (Section 3.3), the general trend shown in Fig. 5 and Fig. S3 would be consistent under different CPC operating conditions.

The five best working fluids were found to be glycerine (G), diethylene glycol (DEG), ethylene glycol (EG), 2-aminoethanol (2AE), and dimethyl phthalate (DMP), achieving the smallest $D_{p,\text{kel},50}$ of 1.56, 1.88, 1.92, 1.98, and 2.10 nm. The $D_{p,\text{kel},50}$ values simulated by the Graetz solution are 1.55, 1.87, 1.91, 1.97, and 2.09 nm, which vary between 0.4 and 0.7% lower (potentially due to the size of the COMSOL mesh), again demonstrating an excellent agreement between these two simulation methods. The activation efficiency curves for the five best working fluids are displayed in Fig. 6. As can be seen, glycerine shows a distinctly smaller $D_{p,\text{kel},50}$ value compared to the other four working fluids. Future experiments are therefore needed to examine the possibility of using glycerine as the working fluid of the CPC, despite its high viscosity. Additional simulation results using c as the variable to solve the convective diffusion equation are displayed in Figs. S4 and S5. They show that the influences of working fluid saturation vapor pressure (p_s) and surface tension (σ) on $D_{p,\text{kel},50}$ are not affected, although the exact values of $D_{p,\text{kel},50}$ decrease when c is used as the variable.

Other than calculating $D_{p,\text{kel},50}$ values as an indicator for the activation of the sub-3 nm particles, we also need to examine whether the activated particles can grow sufficiently to a detectable size so that the particle number can be counted. Using Eqs. (5) and (6), we calculated the growth of the droplets along their trajectory in the condenser (Fig. 7). The condensational growth of 2.1 nm particles was simulated along the centerline ($r = 0$), $r = 0.1R$, and $r = 0.5R$ for the five best working fluids. Except for glycerine, all the other four working fluids were shown to sufficiently grow the particles to sizes above 1 μm . Due to the lower p_s and relatively lower D of the glycerine, the condensational growth of the particles using glycerine as the working fluid is significantly slower, yielding a smaller grown particle size of around 300 nm. However, a second-stage CPC can conveniently detect them. Since diethylene glycol already uses a two-stage CPC, glycerine is a candidate working fluid that can reduce $D_{p,\text{kel},50}$ by approximately 0.3 nm. The calculation also showed that 2-aminoethanol can grow particles to approximately 5.7 μm , meaning that a single-stage CPC will be sufficient to detect the grown sub-3 nm particles.

3.3. Influence of CPC operating condition

The above simulation results show that the COMSOL simulation can generate consistent results on particle detection in CPC. Here we used COMSOL to examine how the CPC operating conditions and geometry may be improved to further enhance the activation of sub-3 nm particles. Here, we used butanol as the working fluid, and varied the values of T_c , Q_c , Q_a , D_c , and L_c , respectively. Among these parameters, T_c , Q_c , and Q_a are associated with the CPC operating conditions, and D_c and L_c are associated with the CPC geometry. The

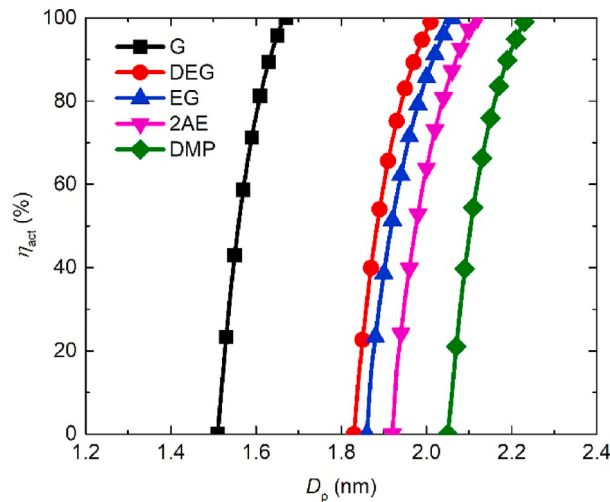


Fig. 6. Simulated activation efficiency curves for the five best working fluids. G, DEG, EG, 2AE, and DMP stands for glycerine, diethylene glycol, ethylene glycol, 2-aminoethanol, and dimethyl phthalate, respectively.

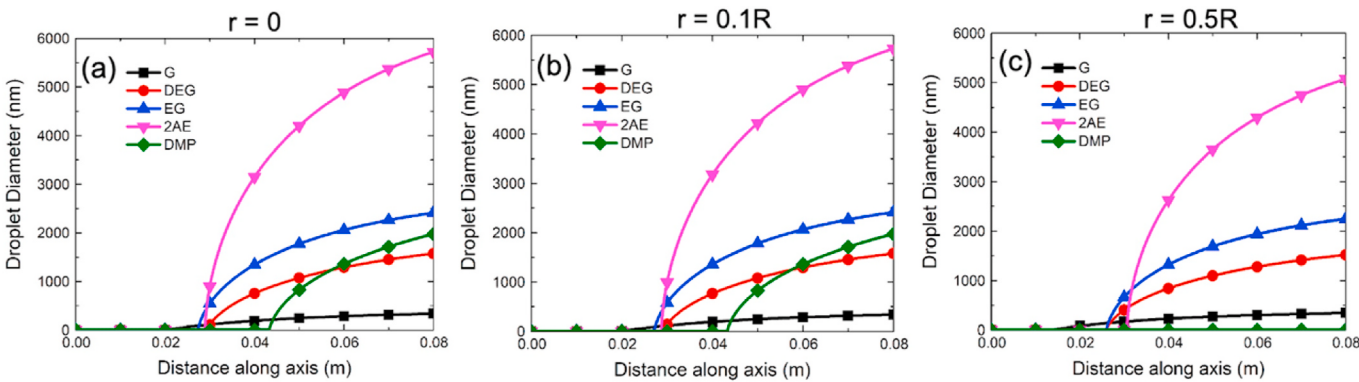


Fig. 7. Droplet size as a function of distance along the axis of CPC using the five best working fluids simulated by COMSOL. G, DEG, EG, 2AE, and DMP stands for glycerine, diethylene glycol, ethylene glycol, 2-aminoethanol, and dimethyl phthalate, respectively. The condensational growth of 2.1 nm particles was simulated (a) along the centerline ($r = 0$), (b) $r = 0.1R$, (c) $r = 0.5R$. Note that DMP particles are not activated effectively at $r = 0.5R$ because of the low saturation ratio.

dependence of η_{act} on these parameters is displayed in Fig. 8. It can be seen that all of these parameters can effectively impact the spectral shape of activation efficiency curves, which are reflected in the change of $D_{p,kel,0}$ and $D_{p,kel,50}$. Conditions that can lead to a lower $D_{p,kel,50}$ value are favored for improving the performance of the CPC.

Among these parameters, a lower T_c and a smaller D_c can lead to decreases in both $D_{p,kel,0}$ and $D_{p,kel,50}$. This is because a lower T_c can reduce the homogeneous nucleation rate more significantly than the condensation rate, thus increasing the temperature difference between the saturator and condenser. As shown previously in Kuang, Chen, McMurry, and Wang (2012), a larger temperature difference between the saturator and condenser ($\Delta T = T_s - T_c$) can lead to a better activation of the sub-3 nm particles. Limited by the freezing point of the working fluid, T_c cannot be decreased indefinitely. Similarly, by reducing the diameter of the condenser, under the same condenser flow rate, the flow speed inside the condenser would increase, reducing the residence time of the condensing vapor. Such a reduction of residence time can suppress homogeneous nucleation, also allowing a higher T_s and ΔT in the saturator. However, the increase of the flow speed will also limit the time for droplet growth as discussed later.

Compared to T_c and D_c values, Q_a only affects the $D_{p,kel,50}$, leaving the $D_{p,kel,0}$ value unchanged. This is due to the supersaturation profile and the largest particle size that cannot be activated in the condenser mainly being determined by the temperature of the saturator flow. A smaller Q_a can lead to a sharper activation efficiency curve, because most of the particles can be constrained in the region with a high supersaturation. This sharper increase of the activation efficiency also leads to a smaller $D_{p,kel,50}$, which improves the performance of the CPC in detecting sub-3 nm particles. This improvement is also the advantage of ultrafine CPCs compared to CPCs with larger cut-off sizes, since in ultrafine CPCs, the aerosol flow through the capillary is shielded by the particle-free air from the saturator. The lower boundary of Q_a is limited by the counting statistics because fewer particles will be detected by the optics. At the same time, a lower Q_a will lead to a larger diffusion loss of particles in the capillary. Q_c and L_c have limited effects in improving the performance of the CPC because the change in $D_{p,kel,50}$ is negligible. Increasing Q_c or decreasing L_c can both lead to a sharper activation efficiency curve by flattening the supersaturation profile around the axis of the condenser (similar supersaturation along the radial direction). Increasing Q_c leads to an increasing deficit of vapor pressure along the centerline of the condenser due to insufficient length of saturator extension. This lower vapor pressure results in an increase of T_s (Fig. 8b) due to the constraint on nucleation rate in the condenser. Thus, $D_{p,kel,50}$ are similar under different values of Q_c because of the balance between vapor pressure and T_s , but particles away from the centerline can be activated with higher efficiency under higher Q_c . Regarding the influence of L_c , a shorter L_c can clip the saturation ratio profile before the peak is achieved along the centerline. Due to the constraint of the nucleation rate in the condenser, a higher T_s can be used for a shorter L_c , and due to the clipping of the peak saturation ratio, the radial distribution of saturation ratio becomes more uniform, flattening the profile of saturation ratio and sharpening the activation efficiency curve.

Although D_c , L_c , and Q_c could pose an influence on particle activation, one needs to note that the effective particle detection depends both on particle activation and droplet growth. Droplets that are not sufficiently grown to detectable sizes, even if they are activated, will not be detected by the optics of the CPCs. The reason for the smaller $D_{p,kel,50}$ at a smaller D_c is that the volume for calculating the homogeneous nucleation in the condenser is smaller, leading to a higher T_s . In order to understand the effects of D_c , L_c , and Q_c on particle activation, we also need to consider the time that allows the activated particle to grow in the condenser (t_g), and this time can be approximated with

$$t_g \sim D_c^2 L_c^* / Q_c \quad (7)$$

where L_c^* represents the length of the condenser beyond the point of activation. Thus, under a same Q_c , to guarantee the same t_g , if D_c is decreased, L_c must be increased, meaning that the nucleation rate will increase accordingly. Moreover, a decreased D_c means an increased flow velocity through the region with high saturation ratio, further leading to the insufficient growth of the droplets. Therefore, D_c and L_c are not independent variables if we consider the growth of particles for further particle detection. Also according to Eq. (7), for a condenser with a fixed geometry, increasing Q_c will reduce t_g , again leading to insufficient growth of the particles. Due to such reasons, to optimize the performance of a single-stage laminar flow CPC, lowering T_c is the most effective approach for enhancing the activation and detection of sub-3 nm particles.

4. Conclusions

In this work, we simulated the sub-3 nm particle activation and growth in a laminar flow CPC using COMSOL coupled with MATLAB data processing. COMSOL simulation showed excellent agreement with the Graetz solution, which was used for examining the performance of ultrafine CPCs in earlier studies. The axial diffusion and incorporation of capillary geometry at the inlet of the saturator extension had limited effect on the simulation results, meaning that the simulation of the CPC performance can be simplified. Using different variables, (i.e., vapor partial pressure or vapor concentration) for solving the convective diffusion equation can lead to significant differences in the simulated activation efficiencies due to the varying temperature field. However, the general trend found in CPC performance is not affected. Our COMSOL simulations show that among 46 commonly used solvents, glycerine, diethylene glycol, ethylene glycol, 2-aminoethanol, and dimethyl phthalate are the five best working fluids, achieving the smallest $D_{p,kel,50}$ of 1.56, 1.88, 1.92, 1.98, and 2.10 nm under a condenser temperature of 10 °C and a condenser flow rate of 0.3 lpm. The values simulated by the analytical Graetz solution range from 0.4% to 0.7% lower, again demonstrating the agreement between these two simulation methods. Particles of 2.1 nm can be effectively grown with these working fluids to a few hundreds of nanometers that can be detected by a second-stage CPC with high efficiencies. Our work shows that lowering the condenser temperature, reducing the diameter of the condenser tube, and using a lower aerosol flow rate through the capillary can enhance the activation of sub-3 nm particles by reducing $D_{p,kel,50}$, while the condenser length and flow rate have limited effect in improving the performance of the CPC. However, if particle

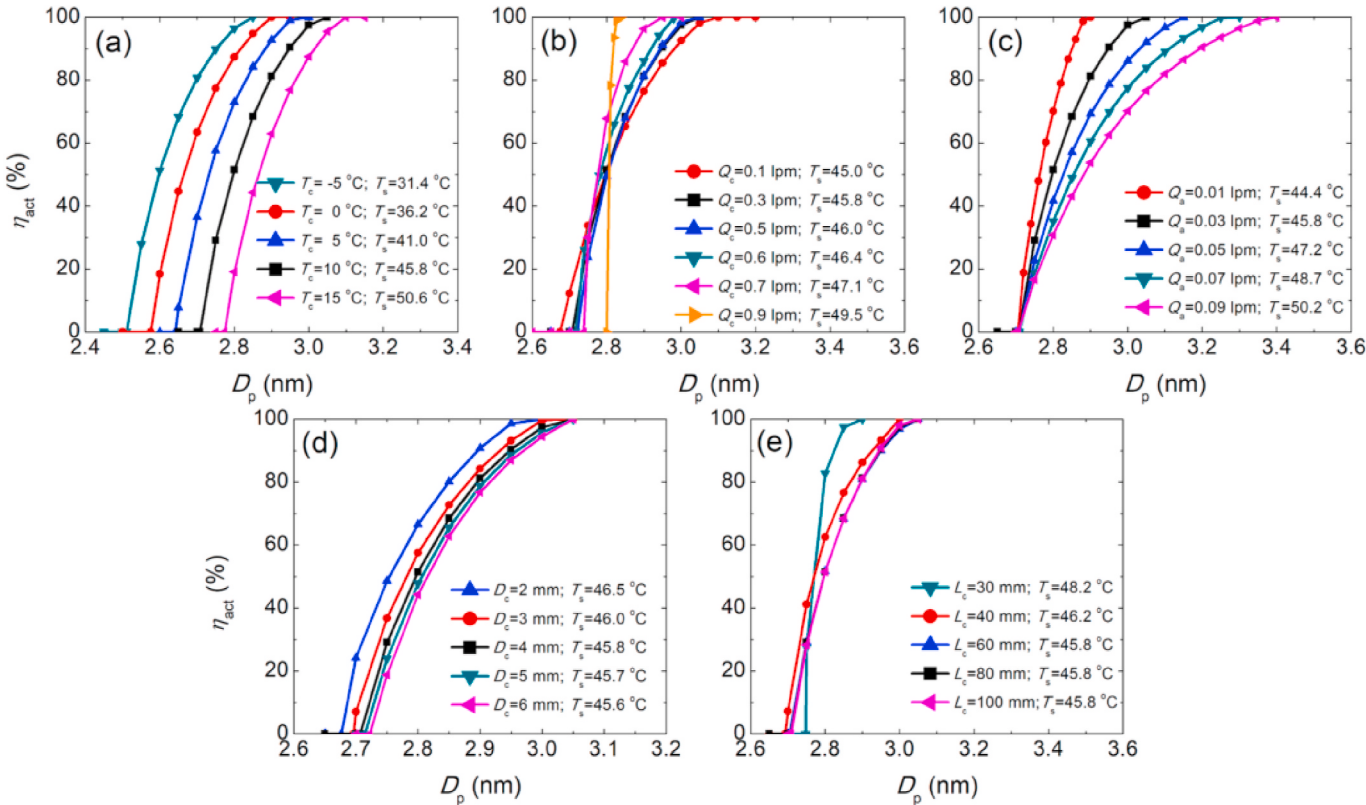


Fig. 8. Dependence of particle activation efficiency on CPC operating conditions and geometry. (a) condenser temperature (T_c), (b) flow rate through the condenser (Q_c , $Q_a = 0.1Q_c$), (c) flow rate through the capillary (Q_a , $Q_c = 0.3 \text{ lpm}$), (d) diameter of the condenser (D_c), (e) length of the condenser (L_c).

growth is considered, lowering the condenser temperature is the most effective approach for enhancing the detection efficiencies of sub-3 nm particles. The use of COMSOL allows for the simulation of CPCs with more complex geometry and flow conditions. Future experimental studies will be conducted to optimize the performance of the CPC further.

Declaration of competing interest

The authors declare that they have no known competing financial interests or personal relationships that could have appeared to influence the work reported in this paper.

Acknowledgements

This work is partially supported by the U.S. National Science Foundation (NSF) Award 2132655.

Appendix A. Supplementary data

Supplementary data to this article can be found online at <https://doi.org/10.1016/j.jaerosci.2021.105841>.

References

- ACS Division of Organic Chemistry. (2020). Common solvents used in organic chemistry. *Table of Properties*. <https://organicchemistrydata.org/solvents/>.
- Atkins, P., & De Paula, J. (2006). *Atkins' physical chemistry* (8th ed.). Oxford Press.
- Attoui, M., & Kangasluoma, J. (2019). Activation of sub 2 nm water soluble and insoluble standard ions with saturated vapors of butanol in a boosted TSI ultrafine CPC. *Atmosphere*, *10*, 665.
- Barmounis, K., Ranjithkumar, A., Schmidt-Ott, A., Attoui, M., & Biskos, G. (2018). Enhancing the detection efficiency of condensation particle counters for sub-2 nm particles. *Journal of Aerosol Science*, *117*, 44–53.
- Becquemin, M., Swift, D., Bouchikhi, A., Roy, M., & Teillac, A. (1991). Particle deposition and resistance in the noses of adults and children. *European Respiratory Journal*, *4*, 694–702.
- Bianchi, F., Tröstl, J., Junninen, H., Frege, C., Henne, S., Hoyle, C. R., Molteni, U., Herrmann, E., Adamov, A., & Bukowiecki, N. (2016). New particle formation in the free troposphere: A question of chemistry and timing. *Science*, *352*, 1109–1112.
- Biswas, P., Wang, Y., & Attoui, M. (2018). Sub-2 nm particle measurement in high-temperature aerosol reactors: A review. *Current Opinion in Chemical Engineering*, *21*, 60–66.
- Butt, H.-J., Graf, K., & Kappl, M. (2013). *Physics and chemistry of interfaces*. John Wiley & Sons.
- Ewing, M., Lilley, T., Olofsson, G., Ratzsch, M., & Somsen, G. (1994). Standard quantities in chemical thermodynamics. Fugacities, activities and equilibrium constants for pure and mixed phases. *Pure and Applied Chemistry*, *66*, 533–552.
- Friedlander, S. K. (2000). *Smoke, dust, and haze*. New York: Oxford University Press.
- Hegg, D. A., & Larson, T. V. (1990). The effects of microphysical parameterization on model predictions of sulfate production in clouds. *Tellus B: Chemical and Physical Meteorology*, *42*, 272–284.
- Hermann, M., Wehner, B., Bischof, O., Han, H.-S., Krinke, T., Liu, W., Zerrath, A., & Wiedensohler, A. (2007). Particle counting efficiencies of new TSI condensation particle counters. *Journal of Aerosol Science*, *38*, 674–682.
- Iida, K., Sakurai, H., Koyama, T., & Taishi, T. (2019). Comparison between dimethyl phthalate and diethylene glycol as a working fluid of a laminar flow particle size magnifier poster presented at. In *37th the American association for aerosol research annual conference*. Oct 14–18; Portland, OR.
- Iida, K., Stolzenburg, M. R., & McMurry, P. H. (2009). Effect of working fluid on sub-2 nm particle detection with a laminar flow ultrafine condensation particle counter. *Aerosol Science and Technology*, *43*, 81–96.
- Jiang, J., Chen, M., Kuang, C., Attoui, M., & McMurry, P. H. (2011). Electrical mobility spectrometer using a diethylene glycol condensation particle counter for measurement of aerosol size distributions down to 1 nm. *Aerosol Science and Technology*, *45*, 510–521.
- Kangasluoma, J., Ahonen, L., Attoui, M., Vuollekoski, H., Kulmala, M., & Petäjä, T. (2015). Sub-3 nm particle detection with commercial TSI 3772 and Airmodus A20 fine condensation particle counters. *Aerosol Science and Technology*, *49*, 674–681.
- Kangasluoma, J., & Attoui, M. (2019). Review of sub-3 nm condensation particle counters, calibrations, and cluster generation methods. *Aerosol Science and Technology*, *53*, 1277–1310.
- Kangasluoma, J., Kuang, C., Wimmer, D., Rissanen, M., Lehtipalo, K., Ehn, M., & Petäjä, T. (2014). Sub-3 nm particle size and composition dependent response of a nano-CPC battery. *Atmospheric Measurement Techniques*, *7*, 689.
- Kuang, C., Chen, M., McMurry, P. H., & Wang, J. (2012). Modification of laminar flow ultrafine condensation particle counters for the enhanced detection of 1 nm condensation nuclei. *Aerosol Science and Technology*, *46*, 309–315.
- Kuang, C., Chen, M., Zhao, J., Smith, J., McMurry, P. H., Wang, J., & Laaksonen, A. (2012). Size and time-resolved growth rate measurements of 1 to 5 nm freshly formed atmospheric nuclei. *Atmospheric Chemistry and Physics*, *12*.
- Lewis, G. S., & Hering, S. V. (2013). Minimizing concentration effects in water-based, laminar-flow condensation particle counters. *Aerosol Science and Technology*, *47*, 645–654.
- Mertes, S., Schröder, F., & Wiedensohler, A. (1995). The particle detection efficiency curve of the TSI-3010 CPC as a function of the temperature difference between saturator and condenser. *Aerosol Science and Technology*, *23*, 257–261.
- Mordas, G., Manninen, H., Petäjä, T., Aalto, P., Hämeri, K., & Kulmala, M. (2008). On operation of the ultra-fine water-based CPC TSI 3786 and comparison with other TSI models (TSI 3776, TSI 3772, TSI 3025, TSI 3010, TSI 3007). *Aerosol Science and Technology*, *42*, 152–158.
- Petäjä, T., Mordas, G., Manninen, H., Aalto, P. P., Hämeri, K., & Kulmala, M. (2006). Detection efficiency of a water-based TSI condensation particle counter 3785. *Aerosol Science and Technology*, *40*, 1090–1097.
- Quant, F., Caldow, R., Sem, G., & Addison, T. (1992). Performance of condensation particle counters with three continuous-flow designs. *Journal of Aerosol Science*, *23*, 405–408.
- Seinfeld, J. H., & Spyros, N. P. (2016). *Atmospheric chemistry and physics: From air pollution to climate change*. John Wiley & Sons, 2016.
- Sem, G. J. (2002). Design and performance characteristics of three continuous-flow condensation particle counters: A summary. *Atmospheric Research*, *62*, 267–294.
- Stolzenburg, M. R. (1988). *An ultrafine aerosol size distribution measuring system*. PhD Thesis. University of Minnesota.
- Stolzenburg, M. R., & McMurry, P. H. (1991). An ultrafine aerosol condensation nucleus counter. *Aerosol Science and Technology*, *14*, 48–65.
- Thomas, J. M., Chen, X., Maißer, A., & Hogan, C. J., Jr. (2018). Differential heat and mass transfer rate influences on the activation efficiency of laminar flow condensation particle counters. *International Journal of Heat and Mass Transfer*, *127*, 740–750.

- Tuch, T., Weinhold, K., Merkel, M., Nowak, A., Klein, T., Quincey, P., Stolzenburg, M., & Wiedensohler, A. (2016). Dependence of CPC cut-off diameter on particle morphology and other factors. *Aerosol Science and Technology*, 50, 331–338.
- Wang, Y., Fang, J., Attoui, M., Chadha, T. S., Wang, W.-N., & Biswas, P. (2014). Application of half mini DMA for sub 2 nm particle size distribution measurement in an electrospray and a flame aerosol reactor. *Journal of Aerosol Science*, 71, 52–64.
- Wang, Y., Kangasluoma, J., Attoui, M., Fang, J., Junninen, H., Kulmala, M., Petäjä, T., & Biswas, P. (2017). The high charge fraction of flame-generated particles in the size range below 3 nm measured by enhanced particle detectors. *Combustion and Flame*, 176, 72–80.
- Wang, Y., Liu, P., Fang, J., Wang, W.-N., & Biswas, P. (2015). Kinetics of sub-2 nm TiO₂ particle formation in an aerosol reactor during thermal decomposition of titanium tetrakisopropoxide. *Journal of Nanoparticle Research*, 17, 1–13.
- Wiedensohler, A., Orsini, D., Covert, D., Coffmann, D., Cantrrell, W., Haylcek, M., Brechtel, F., Russell, L., Weber, R., & Gras, J. (1997). Intercomparison study of the size-dependent counting efficiency of 26 condensation particle counters. *Aerosol Science and Technology*, 27, 224–242.
- Yao, L., Garmash, O., Bianchi, F., Zheng, J., Yan, C., Kontkanen, J., Junninen, H., Mazon, S. B., Ehn, M., & Paasonen, P. (2018). Atmospheric new particle formation from sulfuric acid and amines in a Chinese megacity. *Science*, 361, 278–281.
- Yaws, C. L., & Gabbula, C. (2003). *Yaws' handbook of thermodynamic and physical properties of chemical compounds*. Knovel.